ARCHIVES OF MECHANICS
Arch. Mech. **75** (1-2), 53–73, 2023, DOI: 10.24423/aom.4225

Experimental and numerical investigations on dynamic tensile behavior of a ZrB_2-SiC ceramic

R. HE, J. CAO, K. YANG, L. WANG, D. KONG

College of Civil Engineering, Guizhou University, Guiyang 550025, PR China,
e-mails: 953725345@qq.com (R.Y. He), 1115006391@qq.com (J.X. Cao),
1975240948@qq.com (K.K. Yang),
wanglingling916@sohu.com (L.L. Wang, corresponding author),
dwkong@gzu.edu.cn (D.W. Kong)

The dynamic tensile behavior of a ZrB_2-SiC ceramic was investigated via split Hopkinson pressure bar tests and a bond-based peridynamic model. The experimental results showed that the peak dynamic splitting tensile stress increased linearly with the strain rate. The dynamic tensile stress history and fracture pattern exhibited a significant strain-rate dependence. In simulation, the strain-rate dependent on the critical energy release rate was introduced to predict the dynamic tensile behavior of the ZrB_2-SiC ceramic. The numerical results were in good agreement with the experimental results, verifying the applicability of the peridynamic model. The maximum error of the peak dynamic splitting tensile stress between the experimental and numerical results was no greater than 6%. Moreover, the effect of the strain rate on the fracture patterns of the ZrB_2-SiC ceramic composite can be well predicted by the peridynamics method. The ZrB_2-SiC composite specimen split into two large fragments with additional small fragments under dynamic splitting tension. With the increase of strain rate, the main crack propagation and branching led to a larger fracture region in the middle of the specimen.

Key words: ZrB_2-SiC ceramic, dynamic tensile properties, fracture pattern, strain rate, peridynamic model.

1. Introduction

Ultra-high-temperature ceramics (UHTCs) are appropriate for application in aircraft fuselages, aircraft wing leading edges, and engine blades, owing to their excellent oxidation resistance and high melting point [1–3]. In recent decades, some researchers have focused on the structural design of ZrB_2-based ceramics, such as laminated ZrB_2-SiC ceramics [4], double-layer ZrB_2-based ceramic coatings [5], UHTC corrugated panels [6], and functionally graded ZrB_2-20SiC ceramics [7], to improve their thermal and mechanical properties. Moreover, many researchers have made great efforts to investigate high-temperature me-

chanical properties [8–10], the thermal shock resistance [11–14], and the oxidation resistance [15–17] of UHTCs. It is noted that increasing attention has been paid to the strain-rate dependence and the nonlinear dynamic mechanical behavior of ceramic materials [18–20]. Indeed, the mechanical behavior of ZrB_2-based UHTCs exhibits significant strain-rate dependence under dynamic loading using split Hopkinson pressure bar (SHPB) experiments, including the dynamic strength, nonlinear stress-strain relationship, and fracture modes [21–24]. Moreover, to fully understand the dynamic behavior, a simulation approach was used to predict the dynamic mechanical behavior of ceramics using mechanical models and numerical methods. Wang *et al.* [25] developed a full-scale model using the ABAQUS finite element software to predict the dynamic stress distribution and damage evolution of alumina ceramics. Li *et al.* [26] conducted numerical simulations to characterize the dynamic compression of A95 ceramic materials at high strain rates. Chang *et al.* [27] used the JH-2 model to simulate the impact compression of the A95 ceramic plate. Huang *et al.* [23] predicted the dynamic tension of ZrB_2-SiC ceramic using the modified JH-2 constitutive model. However, traditional numerical methods, such as finite element methods, are based on the local theory and limited by the singularity of the crack tip, which means that it is difficult to simulate the dynamic failure crack propagation of brittle materials without presetting the propagation direction and path of cracks.

The peridynamics theory, owing to its spontaneous nature of crack formation, has unique advantages in analyzing the initiation and propagation of cracks [28, 29], especially the failure behavior when subjected to impact loading [30–32]. The peridynamics model has been successfully applied to simulate dynamic crack propagation and branching, as well as fracture mechanisms [33–37]. Jia *et al.* [38] first simulated the wave propagation via SHPB with the peridynamics model, but they ignored the wave dispersion analysis and the impact failure of specimens. Gu *et al.* [39] found that the numerical dispersion in one dimension can be effectively reduced in the improved prototype microelastic brittle (PMB) model and simulated the failure pattern of a concrete Brazilian disc in via SHPB. However, the model generated a rectangular wave and the results were not verified by experiments. Ai *et al.* [40] investigated the dynamic fracture properties and crack propagation of rock under different SHPB impact loading rates. Therefore, the validity of both method and model needs to be verified with experimental data of materials.

In this study, the dynamic splitting tension of the ZrB_2-SiC ceramic was investigated via SHPB experiments and the discontinuous Galerkin (DG) formulated the peridynamic model. The basic theory of bond-based peridynamics was introduced, and the numerical model and modeling method were described. The peak dynamic splitting tensile stress, tensile stress history, and fracture mode of

the ZrB_2-SiC ceramic were investigated by experimental and numerical methods. A comparison between experimental and numerical results was discussed at different strain rates to show the validity of the peridynamics model.

2. Experimental procedure

The dynamic splitting tensile test was used to measure the tension behavior of a ZrB_2-SiC composite under impact loadings. To conduct the dynamic splitting tests of the ZrB_2-SiC composite, the Split Hopkinson Pressure Bar (SHPB) impact system, which located in the Northwestern Polytechnical University, China, was utilized. The experimental system has three major subsystems: dynamic impact loading system, bars and waveform collection system. In particular, a high-frame and high-resolution camera were employed to record impact videos. The type of high-precision resistance strain gauge used in the tests is BF120-3AA, and its resistance and the sensitivity factor is 119 Ω and 2.19 respectively. The strain gauge was affixed to the specimen with 502 glue.

The schematic diagram of the SHPB system in the splitting tension experiments is shown in Fig. 1.

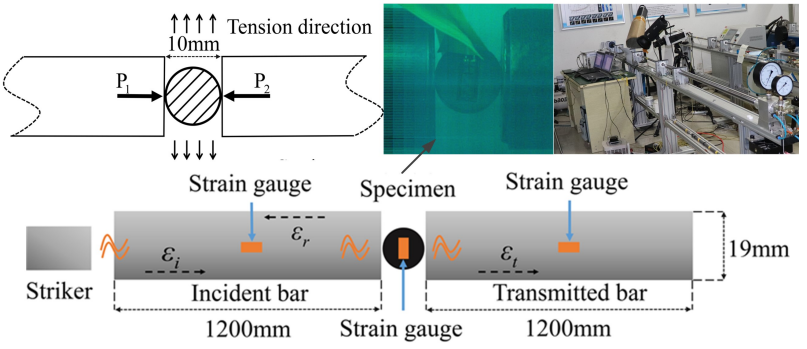

FIG. 1. Schematic diagram of the splitting tension test in the SHPB system.

The incident and transmitted bar was 1200 mm in length and 19 mm in diameter with the density of 7850 kg/m^3, Young's modulus of 190 GPa and Poisson's ratio of 0.3. The ZrB_2-SiC specimen was held between the incident and transmitted bar, and a strain gauge was mounted at the center of the specimen to record the strain along the tension direction. A wave signal was captured by strain gauges on the incident and transmitted bar. Based on the one-dimensional stress wave theory, the dynamic forces on the interface between the incident bar and the sample (P_1), as well as the interface between the transmitted bar and the sample (P_2), can be calculated by the incident, reflected, and transmitted strain $\varepsilon_i(t)$, $\varepsilon_r(t)$, and $\varepsilon_t(t)$ [41]:

$$P_1(t) = AE[\varepsilon_i(t) + \varepsilon_r(t)], \quad P_2(t) = AE\varepsilon_t(t), \tag{2.1}$$

$$P(t) = \frac{P_1(t) + P_2(t)}{2}. \tag{2.2}$$

The dynamic splitting tensile stress of the ZrB_2-SiC ceramic specimen under impact loading can be expressed as

$$\sigma_{ST}(t) = \frac{2P(t)}{\pi DB}, \tag{2.3}$$

where $P(t)$ is the load force, D is the diameter of the specimen, and B is the thickness of the specimen. When the load force $P(t)$ reaches the maximum value $P_{\max}$, the corresponding splitting tensile stress reaches the peak stress of the specimen.

3. Theory and model

3.1. Bond-based peridynamics theory and model

The peridynamics was developed by Silling as a nonlocal theory under the framework of continuum mechanics [28]. In the peridynamics theory, one material point interacts with other material points within the infinite range δ called the horizon The interaction between material points is described by solving spatial integral equations rather than the partial differential equations in traditional finite element methods. The equation of motion for the bond-based peridynamics model is given as [29]

$$\rho\ddot{u}(x,t) = \int_{H_x} f(\eta,\xi)\, dV_{x'} + b(x,t), \tag{3.1}$$

where ρ is the mass density, $\ddot{u}$ is the acceleration at time t, and b is the body force density of the material point x. As shown in Fig. 2, H_x is the neighborhood of material point x, which is defined as

$$H_x(x,\delta) = \{x' \in R : \|x' - x\| \le \delta\};$$

ξ is introduced to denote the relative position between material point x and x' as $\xi = x - x'$. Accordingly, the relative displacement η is defined as $\eta = u(x',t) - u(x,t)$, where $u(x,t)$ and $u(x',t)$ are the displacement of the material point x and x', respectively; $f(\eta,\xi)$ is called the pairwise force or bond force, and it is determined by the displacement of two points.

The function of pairwise force for prototype microelastic brittle (PMB) materials was proposed by Silling and Askari as follows [29]:

$$f(\eta,\xi) = \frac{\partial w(\eta,\xi)}{\partial \eta}, \tag{3.2}$$

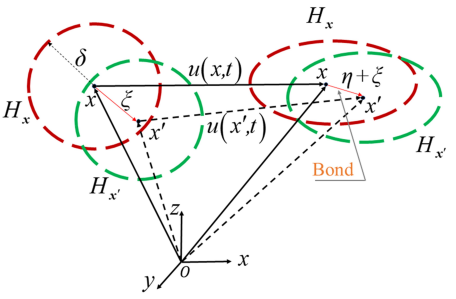

FIG. 2. Schematic diagram of the pairwise interaction of peridynamic bonds.

where $w(\eta,\xi)$ denotes the strain energy per unit volume of a PMB bond. In linear isotropic cases, Poisson's ratio of PMB material is limited to $1/4$ in three-dimensional (3D) problems and the value of the micropotential $w(\eta,\xi)$ depends on the deformation of a bond [28]:

$$w(\eta,\xi) = \frac{cs^2\|\xi\|}{2}, \tag{3.3}$$

where c is the elastic stiffness of a bond called the microelastic modulus, and s is the bond stretch ratio calculated by

$$s(\eta,\xi) = \frac{\|\eta+\xi\| - \|\xi\|}{\|\xi\|}. \tag{3.4}$$

The limitation of the stretch of a bond is called the critical stretch S_0, which is the failure criterion of the bond-based model. It has been said that a bond breaks when the stretch reaches the critical value s_0, and a crack propagates when all of the bonds crossing the path are broken. The critical stretch is related to a measurable fracture mechanics quantity: the critical energy release rate G_c. The relation between G_c and s_0 in 3D problems is given as

$$G_c = \frac{\pi c s_0^2 \delta^5}{10}. \tag{3.5}$$

To define the connection state of each bond a scalar history-dependent function μ is given as

$$\mu(\eta,\xi,t) = \begin{cases} 1, & s \le s_0, \\ 0, & s > s_0. \end{cases} \tag{3.6}$$

Taking the bond-break into consideration, the bond force is calculated by

$$f(\eta,\xi) = cs(\eta,\xi)\mu(\eta,\xi,t)\frac{\eta+\xi}{\|\eta+\xi\|}. \tag{3.7}$$

The damage of a material point can be defined as the following equation:

$$\phi(x,t) = 1 - \frac{\int_{H_x} \mu(x,\xi,t)\, dV_\xi}{\int_{H_x} dV_\xi}. \tag{3.8}$$

The bond-based peridynamics model has been applied to simulate various damage and failure problems of concrete [39], rock-like [40, 41], and composite materials [42–44]. Therefore, the effectiveness and feasibility of the bond-based peridynamics method have been verified in these above studies. However, in this method, it is challenging to identify the applications of boundary conditions. Fortunately, a peridynamics governing equation of the discontinuous Galerkin method, exhibiting advantages of FEM in mesh and boundary condition enforcement, has been presented to investigate some quasi-static and dynamic problems in several studies [45–47].

The bond-based peridynamics governing equation formulated by the DG method is

$$\begin{aligned}\sum_{g=1}^{ng} \rho N^B(x^g)\Delta V^g \ddot{u}_i^B &= \sum_{g=1}^{ng}\Big(\sum_{g'=1}^{ng'} f_i(\eta(x^g,x^{g'}),\xi(x^g,x^{g'}))\Delta V^{g'}\Big)N^B(x^g)\Delta V^g \\ &\quad + \sum\nolimits_{g=1}^{ng} b_i(x^g)N^B(x^g)\Delta V^g,\end{aligned} \tag{3.9}$$

where ng denotes the total number of Gaussian points x^g in the domain, and ng' is the total neighbor Gaussian points $x^{g'}$ of Gaussian points x^g, and N^B is the FEM shape function.

Furthermore, Ren *et al.* [48] utilized the equivalent strain energy to establish the relation between the microelastic modulus and the critical bond stretch. The relation between the elastic modulus$E$ and microelastic modulus C_x is derived as

$$3E = \sum_{\xi} \frac{1}{2} C_x \|\xi\| \Delta V_{x'}, \tag{3.10}$$

where microelastic modulus C_x is a distributive quantity depending on the location of a point x and is calculated by

$$C_x = C_x^0 \sqrt{\left(\frac{1}{(\cos(\theta)\sin(\phi))^2} + \frac{1}{(\sin(\theta)\sin(\phi))^2} + \frac{1}{(\cos(\phi))^2}\right)}, \tag{3.11}$$

where C_x^0 is estimated by Eq. (3.10), and θ and φ are the spherical coordinates, respectively.

3.2. Numerical model

The bond-based peridynamic model implemented in Ls-DYNA is conducted in the FEM framework with the discontinuous Galerkin theory. *SECTION_SOLID_PERI is used to define the peridynamic section keyword. ELFORM= 48 is set as the element formulation number of the bond-based peridynamics model. *MAT_ELASTIC_PERI is another keyword used to define an elastic mechanical behavior for brittle materials. Density, elastic modulus and fracture energy release rate are the main parameters that should be defined in this keyword. Comparing with the regular FEM mesh, peridynamic mesh uses discontinuous mesh. The elements do not share nodes like the regular FEM mesh, and each element has its own nodes index. As shown in Fig. 3, the discontinuous elements can be obtained from the regular FEM mesh by detaching nodes in Ls-Prepost.

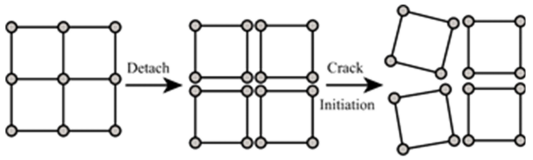

(a) Discontinuous Galerkin finite element

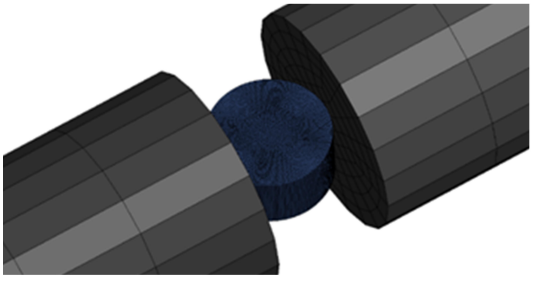

(b) Diagram of Brazil disk specimen element

FIG. 3. Schematic view of element type in Ls-dyna.

A Brazil disk splitting specimen made of ZrB_2-SiC ceramic and the SHPB device was modeled using the finite element software Ls-dyna. The length and diameter of the incident bar and transmitted bar were 1200 mm and 19 mm, respectively, which were in the same size in the experiments. The elastic constitutive model *MAT_ELASTIC was used to describe the properties of the steel bar. Moreover, to effectively output the incident wave and transmitted wave signal, as well as to reduce the computing time, two bars were meshed into a total of 25 200 hexahedral elements. A sine wave, which was fitted by the experimental stress waves under different strain rates as shown in Fig. 4, was loaded on the end of the incident bar to ensure that the loading conditions of the simulation were consistent with those in the tests. The keyword *CONTACT_AUTOMATIC_

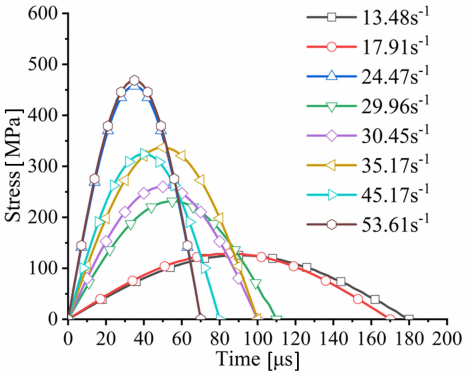

FIG. 4. The stress waves loaded on the incident bar.

SURFACE TO SURFACE was selected to simulate the interaction between the steel bars and ceramic specimens.

In Ls-dyna, bond-based Peridynamics theory was implemented under the DG framework. The nodes of each element are disconnected so that cracks initiate along the elemental contact surfaces when bonds break rather than via element deletion. In the simulation, the Brazil disk specimen made of the ZrB_2-SiC ceramic was discretized with 120000 elements in a mesh type of ELFORM48, and the horizon radius δ was determined by the diagonal length of each element l_e ($\delta = 1.01 l_e$).

The parameters of the ZrB_2-SiC ceramic specimen in the numerical simulation are listed in Table 1.

TABLE 1. The parameters of specimen in the numerical simulation.

Diameter [mm]	Thickness [mm]	ρ [kg/m^3]	E [GPa]
10	5	4750	500

In simulation, the energy release rate is an important parameter to control the progress of crack propagation in brittle materials. Damage and cracking occur when the sum of the work to break all the bonds within a region exceeds a critical amount, which is known as the critical energy release rate. For brittle fracturing, the critical energy release rate G_c can be derived from linear elastic fracture mechanics as follows [49]:

$$G_c = \frac{K_{IC}^2(1-\upsilon^2)}{E}, \tag{3.12}$$

where K_{IC} is the fracture toughness of the material.

It is noted that an obvious strain-dependent tensile and compressive behavior of ZrB_2-based ceramics has been pointed out in existing studies [22–24]. Moreover, some studies have illustrated that dynamic fracture toughness of brittle materials increase with an increasing loading rate [49, 50]. Therefore, in the present study, the critical energy release rate G_c is considered to have a correlation with the strain rate in the dynamic tensile behavior of the ZrB_2-SiC ceramics. To illustrate the strain rate dependence on the energy release rate, the expression of dynamic critical energy release rate $G_{dc}(\dot{\varepsilon})$ can be written as

$$G_{dc}(\dot{\varepsilon}) = K_{ID}(\dot{\varepsilon}) \cdot (1 - \upsilon^2)/E. \tag{3.13}$$

4. Results and discussion

4.1. Experimental results

In the splitting tensile tests, the tension direction was perpendicular to the loading direction. The strain rate of the specimen was calculated by the slope of the strain-time curve from the data recorded by the strain gauge at the center of the specimen, as shown in Fig. 5.

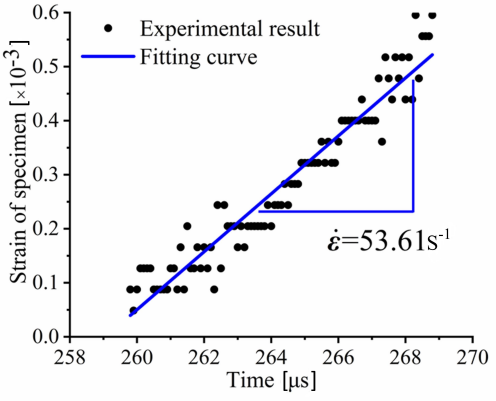

FIG. 5. The strain rate calculated by the strain-time curve at $53.61\,s^{-1}$.

In this study, SHPB impact experiments of the ZrB_2-SiC specimen were conducted with the strain rate ranging from 13.48 to $53.61\,s^{-1}$. Wave signals were recorded by the strain gauges on the incident and transmitted bar, and the incident, reflected, and transmitted waves at the strain rate of $53.61\,s^{-1}$ were extracted, as shown in Fig. 6.

It can be seen that the stress equilibrium was met in the dynamic splitting tensile test. However, a sudden increase in signal appeared in the reflected wave due to the failure and the sudden loss of load-bearing capacity of the specimen.

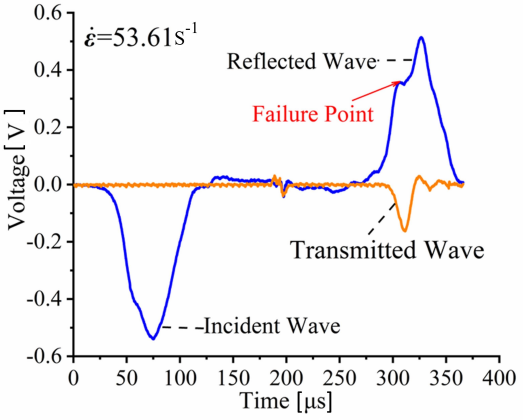

FIG. 6. Incident, reflected, and transmitted waves at the strain rate of 53.61 s^{-1}.

Figure 7 summarizes the peak splitting tensile stress of the ZrB_2-SiC composite over the strain rate of 13.48 to 53.61 s^{-1}. As shown in Fig. 8, the peak splitting tensile stress of the ZrB_2-SiC ceramic was 230.85 MPa at 13.48 s^{-1}, while that at 53.61 s^{-1} was 498.14 MPa. It can be seen from the test results that the tensile properties of ZrB_2-SiC composites have a correlation with the strain rate. Moreover, a linear relationship between the peak splitting tensile stress and strain rate was observed, which evidently showed the dependence of peak splitting tensile stress on the strain rate. The material exhibits an obvious strain rate effect that its ability to withstand ultimate load increases with the increase of the strain rate. The main reason is that with the increase of the impact gas

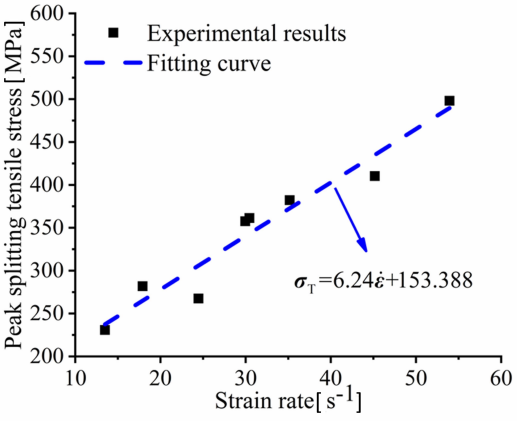

FIG. 7. Peak splitting tensile stress of ZrB_2-SiC ceramics under different strain rates.

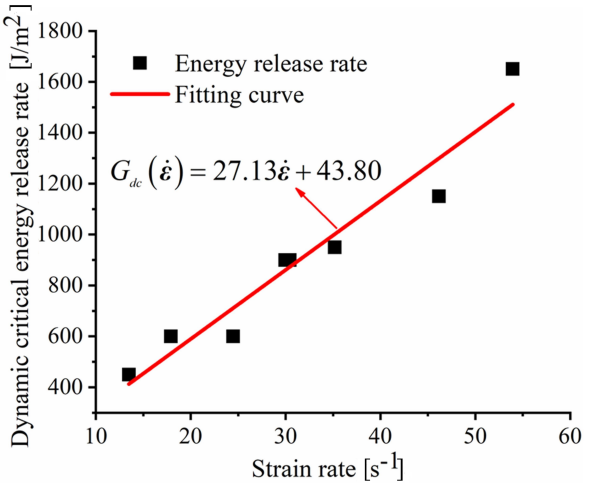

FIG. 8. Strain-rate dependent critical energy release rate.

pressure, the impact load increases. The micro-cracks inside the sample have no time to crack and expand, and the deformation seriously lags behind the stress, causing the increase of the dynamic tensile strength.

4.2. Numerical results

The finite element model and bond-based peridynamics model were presented using the Ls-dyna software. The effect of a strain rate on the fracture behavior of the ZrB_2-SiC ceramic was considered in the present simulation. The quasi-static fracture toughness of the ZrB_2-SiC composite was located in the range from 4.40 to 4.96 MPa $\cdot$ m$^{1/2}$ [51–55]. The average value 4.68 MPa $\cdot$ m$^{1/2}$ was used to calculate the quasi-static critical energy release rate (43.80 J/m^2) in Eq. (3.12). On that basis, a strain-rate dependent dynamic critical energy release rate $G_{dc}(\dot{\varepsilon})$ was utilized to predict the dynamic tensile behavior of the ZrB_2-SiC ceramic. The value of the dynamic critical energy release rate in Fig. 8 was the key parameter affecting the simulation results. The value of this strain-rate dependent critical energy release rate in simulation was determined by comparing the stress curves of experimental and numerical results under different strain rates. The correlation between the dynamic critical energy release rate $G_{dc}(\dot{\varepsilon})$ and the strain rate $\dot{\varepsilon}$ in this work is listed in Fig. 8. A clear linear increase in the critical energy release rate with strain rate was found, and this linear correlation validated our consideration of the strain-rate dependence on the energy release rate. The equation was fitted as follows

$$G_{\mathrm{dc}}(\dot{\varepsilon}) = 27.13\dot{\varepsilon} + 43.80. \tag{4.1}$$

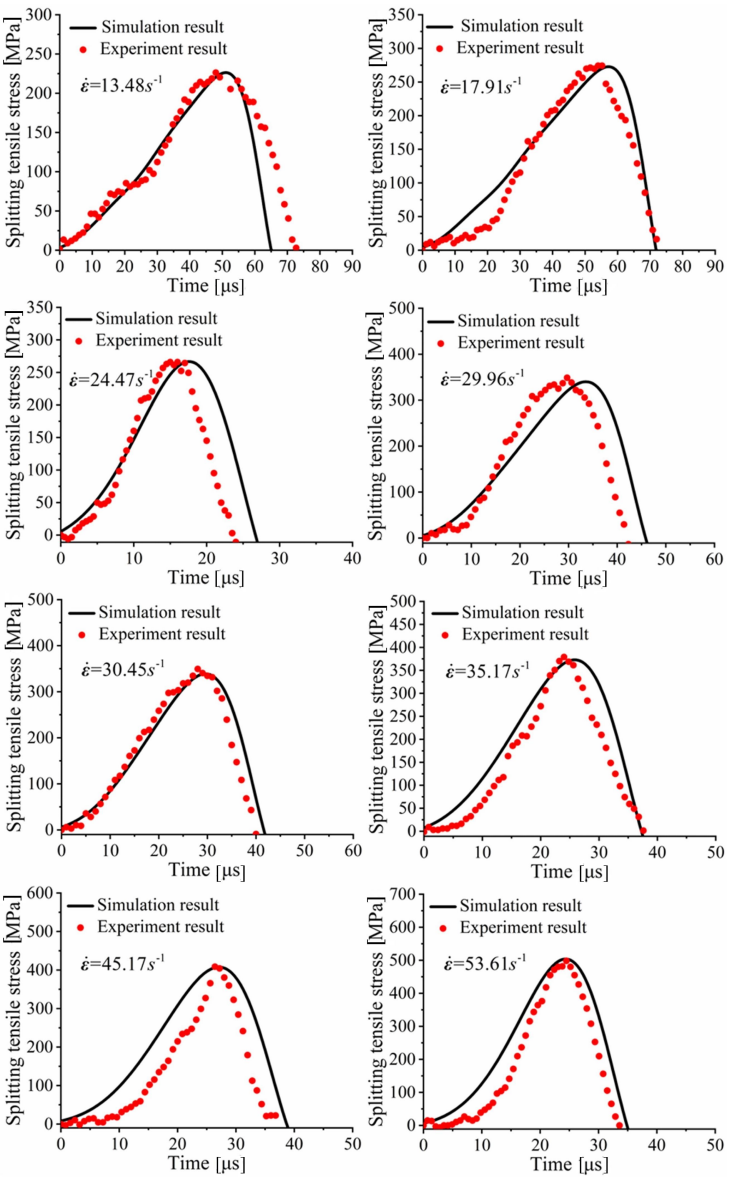

Fig. 9. Splitting tensile stress-time curves between the peridynamics simulation and experiment under different strain rates.

The dynamic splitting tensile stress history from simulation under different strain rates is listed in Fig. 9.

The Ls-prepost software was used to output the strain wave of the incident and transmitted bars, and the splitting tensile stress of the specimen was calculated using Eq. (2.3). From Fig. 9, the peak splitting tensile stress and stress-time

curve from the peridynamics simulation were approximately consistent with the experimental tests. The comparison results exhibited a good consistency between the numerical and experimental data. This indicated that the bond-based DG formulated peridynamic model can well predict the strain-rate dependent tensile behavior of the ZrB_2-SiC ceramic.

As shown in Fig. 10, the predicted peak dynamic splitting tensile stress was consistent with the experimental values. Comparing the simulated results with the experimental results, the maximum error between the experimental and numerical peak stress recorded in Table 2 is no more than 6%.

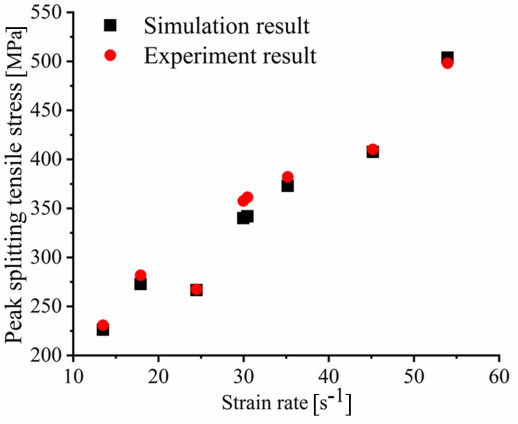

FIG. 10. Comparison of peak splitting tensile stress between experiment and simulation.

TABLE 2. The comparison of the peak splitting tensile stress between experiment and simulation.

Strain rate [s^{-1}]	Experimental peak stress [MPa]	Simulated peak stress [MPa]	Error rate [%]
13.48	230.85	226.29	1.98
17.91	281.81	272.80	3.2
24.47	267.48	266.72	0.28
29.96	357.65	340.10	4.90
30.45	361.34	341.96	5.36
35.17	382.16	372.96	2.41
45.17	410.25	407.64	0.64
53.61	498.14	503.83	1.14

The peak dynamic splitting tensile stress increased linearly with increasing strain rate. In this study, the dependence of the critical energy release rate was utilized in the simulation, which caused the numerical results to exhibit strong

consistency with the experimental data. Therefore, the dependence of fracture behavior on strain rate needs to be considered in the simulation of dynamic mechanical behavior. Comparing the splitting stress history and the peak splitting tensile stress verified the applicability of the peridynamic model to predict the dynamic splitting tensile behavior of the ZrB_2-SiC composite.

In this study, the fracture process under different strain rates was obtained to fully understand the dynamic behavior and failure mechanism of the ZrB_2-SiC ceramic. As shown in Fig. 11, comparing the failure patterns from peridynamics simulation with experimental results, a good agreement was observed at strain rates of 13.48, 17.91, and 24.47 s^{-1}. The ZrB_2-SiC specimen was broken into two large fragments with additional small fragments. The main fracture region was located in the middle part of the ZrB_2-SiC specimen, and a main crack propagated along the loading direction. Additionally, it was found that the damage along the loading direction became more serious with the increase of strain rate.

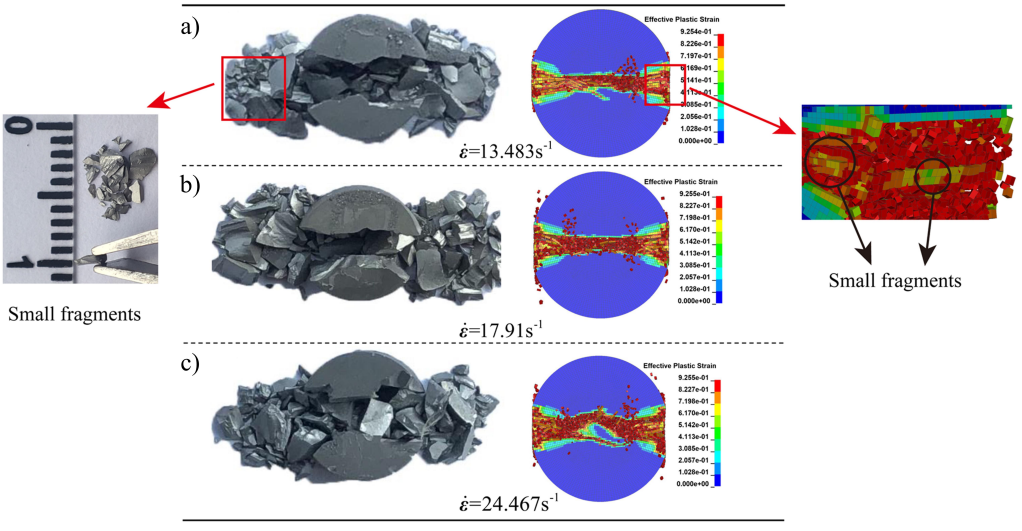

Fig. 11. Dynamic fracturing patterns of the ZrB_2-SiC specimen at strain rates of (a) 13.48 s^{-1}, (b) 17.91 s^{-1}, (c) 24.47 s^{-1}.

Figure 12 shows the crack propagation process of the ZrB_2-SiC specimen at the strain rate of 13.48 s^{-1}. It can be found that, when the impact pulse reached the interface between the ZrB_2-SiC specimen and incident bar, the damage firstly appeared at the specimen contact ends. Owing to the tensile strength of ceramic being much lower than its compressive strength, a slight damage and fracture occurred at both ends of the specimen, which caused the initiation and propagation of the main crack along the loading direction. Therefore, Fig. 12 shows that

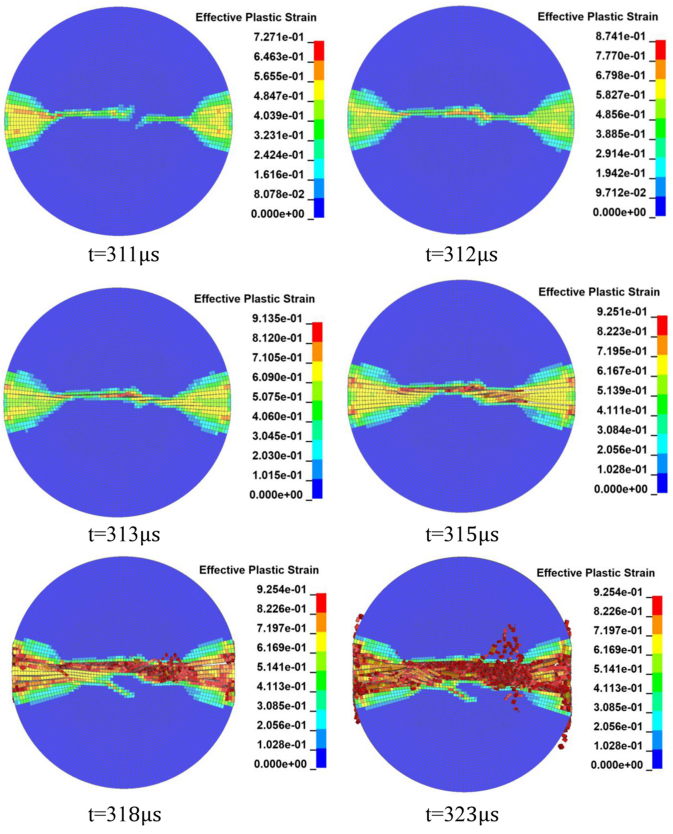

FIG. 12. Failure process of the ZrB_2-SiC ceramic disk at a strain rate of $13.48\,s^{-1}$.

the fracture started near the contact ends of the specimen, and a crack initiated from the contact end and moved along the loading direction. Then, the crack at two contact ends converged to penetrate the specimen. Under the splitting tension condition, the tensile stress perpendicular to the direction of the stress wave caused the generation and propagation of a main crack, which resulted in a model-I fracture of the ceramic specimen. Moreover, the width of the nucleation of the crack increased under dynamic impact loading with increasing time, which made the specimen split into two main parts with additional, small fragments.

In the present study, the peridynamic model was applied to predict the dynamic fracture process of a ZrB_2-SiC ceramic specimen under splitting tension. Figure 13 shows the dynamic splitting tensile fracture process of the ZrB_2-SiC specimen via peridynamic simulation at strain rates of 29.96, 35.17, 45.17, and $53.61\,s^{-1}$. An effective plastic strain was introduced to evaluate the damage of the specimen, and the fracture region increased with the strain rate, as seen in

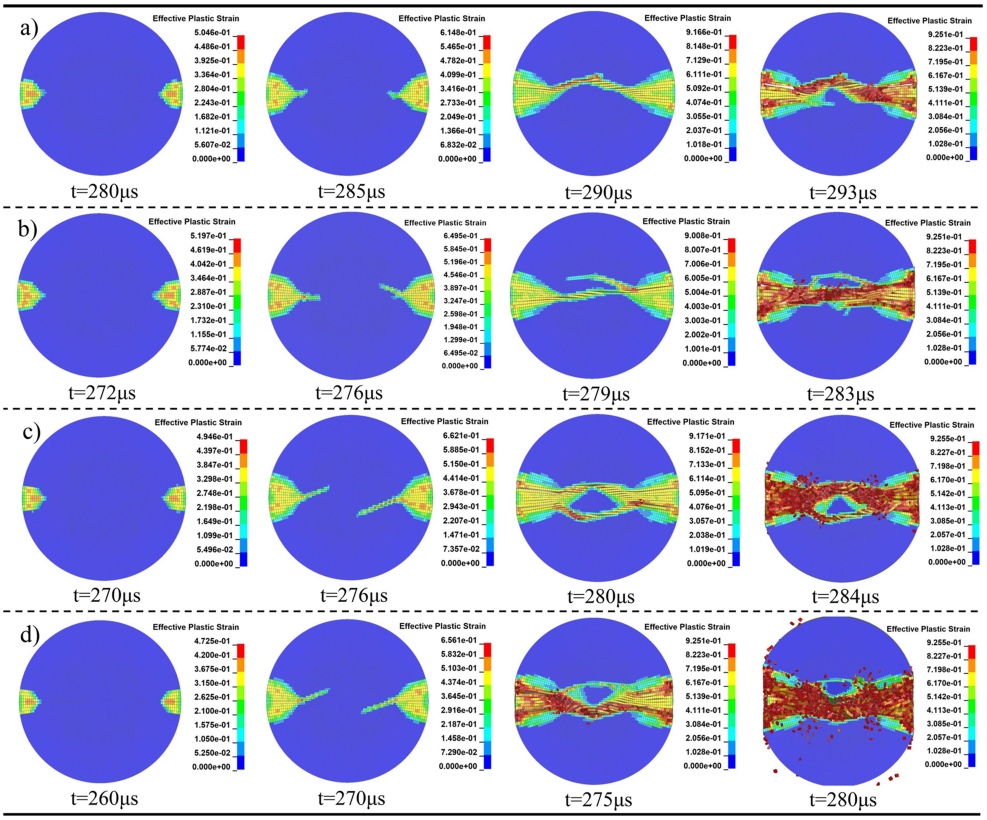

FIG. 13. Dynamic tensile fracturing pattern of the ZrB_2-SiC specimen at different strain rates: (a) 29.96 s^{-1}, (b) 35.17 s^{-1}, (c) 45.17 s^{-1}, (d) 53.61 s^{-1}.

Fig. 13. Moreover, it was obvious that the initiation and propagation of the central main crack parallel to the loading direction was the main fracture pattern of the ZrB_2-SiC ceramic specimen. Furthermore, compared with the fracture process at a strain rate of 13.48 s^{-1}, more branching cracks were generated in the tensile region of the specimen at relatively high strain rates. As the strain rate increased, more branching cracks generated from both ends of the specimen and propagated to the center along the loading direction. This fracture pattern caused the ZrB_2-SiC specimen to break into two main fragments with additional small fragments. With the increase of strain rate, the fracture region increased, and more crack nucleation appeared in the splitting specimen. The peridynamic simulation results evidently suggested the effect of strain rate on the fracture process of the ZrB_2-SiC ceramic under dynamic splitting tension. Therefore, more cracks could consume more energy at higher strain rates, which led to the increase in splitting tensile stress. This was consistent with the conclusion that

peak dynamic splitting tensile stress rose with an increasing strain rate. Overall, the strain-rate dependent dynamic splitting tensile behavior of ZrB_2-SiC ceramic can be well predicted using the bond-based peridynamics model. The simulation results of tensile stress-time trends, dynamic splitting tensile stress, and dynamic fracture pattern exhibited good accordance with the experimental results.

5. Conclusion

In this study, the dynamic splitting test via the SHPB device and the DG formulated peridynamic model were applied to investigate the dynamic splitting tensile behavior of ZrB_2-SiC ceramic. The effects of strain rate on peak splitting tensile stress and the fracture pattern were understood through experimental and numerical results. The main conclusions are summarized as follows:

(1) ZrB_2-SiC ceramic exhibited a significant strain-rate dependence under dynamic splitting tension from 13.48 to 53.61 s^{-1}. A comparison between the experimental and numerical results demonstrated that the peridynamic model can well predict the tensile stress-time history and peak splitting tensile stress of the ZrB_2-SiC ceramic.

(2) In simulation, the critical energy release rate was utilized to determine the critical bond stretch s_0. The strain-rate dependent critical energy release rate $G_{dc}(\dot{\varepsilon})$ was introduced in the peridynamic model. When the critical energy release rate linearly increased with a strain rate, the numerical result of splitting tensile stress showed good accordance with the experimental results of the ZrB_2-SiC ceramic.

(3) The fracture pattern and process of the ZrB_2-SiC ceramic composite can be well predicted by the DG formulated peridynamic model. A crack started from the contact end and propagated near the center of the specimen along the loading direction. With the increase of the strain rate, the main crack propagation and branching led to a larger fracture region. The ZrB_2-SiC ceramic specimen split into two large fragments with additional, small fragments under dynamic splitting tension.

Acknowledgements

This work was supported by the National Natural Science Foundation of China [Grant No. 12162009], the Science and Technology Planning Project of Guizhou Province [Grant No. [2020]1Y244], the Cultivation Project of Guizhou University [Grant No. [2019]28], and the Civil Engineering First-Class Discipline Construction Project of Guizhou Province [Grant No. QYNYL[2017]0013]. We thank LetPub (www.letpub.com) for its linguistic assistance during the preparation of this manuscript.

Data availability statement

All data, models, or codes that support the findings of this study are available from the corresponding author upon reasonable request.

References

1. F. Monteverde, A. Bellosi, L. Scatteia, *Processing and properties of ultra-high temperature ceramics for space applications*, Materials Science and Engineering, A **485**, 1–2, 415–421, 2008.
2. T.H. Squire, J. Marschall, *Material property requirements for analysis and design of UHTC components in hypersonic applications* Journal of the European Ceramic Society, **30**, 11, 2239–2251, 2010.
3. R. Savino, L. Criscuolo, G.D. Di Martino, S. Mungiguerra, *Aero-thermo-chemical characterization of ultra-high-temperature ceramics for aerospace applications*, Journal of the European Ceramic Society, **38**, 8, 2937–2953, 2018.
4. X.F. Ma, C.C. Wei, R.X. Liu, S. Li, Z.Y. Zhang, L.Y. Liu, P. Wang, Y.S. Wang, *Ablative properties of laminated ZrB_2-SiC ceramic modified by SiC whisker in oxyacetylene environment*, Corrosion Science, **182**, 109283, 2020.
5. B.S. Xu, R.J. He, C.Q. Hong, Y.B. Ma, W.B. Wen, H.M. Li, T.B. Cheng, D.N. Fang, Y.Z. Yang, *Ablation behavior and mechanism of double-layer ZrB_2-based ceramic coating for lightweight carbon-bonded carbon fiber composites under oxyacetylene flame at elevate temperature*, Journal of Alloys and Compounds, **702**, 551–560, 2017.
6. K. Wei, R.J. He, X.M. Cheng, R.B. Zhang, Y.M. Pei, D.N. Fang, *A lightweight, high compression strength ultra high temperature ceramic corrugated panel with potential for thermal protection system applications*, Materials & Design, **66**, 552–556, 2015.
7. A. Nisar, M.M. Khan, K. Balani, *Enhanced thermos-mechanical damage tolerance of functionally graded ZrB_2-20SiC ceramic reinforced with carbon nanotubes*, Ceramics International, **45**, 5, 6198–6208, 2019.
8. M. Lugovy, V. Slyunyayew, N. Orlovskaya, E. Mitrentsis, C.G. Aneziris, T. Graule, J. Kuebler, *Temperature dependence of elastic properties of ZrB_2-SiC composites*, Ceramics International, **42**, 2, 2439–2445, 2016.
9. P. Hu, Z. Wang, *Flexural strength and fracture behavior of ZrB_2-SiC ultra-high temperature ceramic composites at 1800° C*, Journal of the European Ceramic Society, **30**, 4, 1021–1026, 2010.
10. R.Z. Wang, W.G. Li, D.Y. Li, D.N. Fang, *A new temperature dependent fracture strength model for the ZrB_2-SiC composites*, Journal of the European Ceramic Society, **35**, 10, 2957–2962, 2015.
11. X. Yue, X.H. Peng, Z. Wei, X.S. Chen, T. Fu, *Effect of heating rate on the strength of ZrB_2-SiC composites subjected to cyclic thermal shock*, Ceramics International, **45**, 12, 15400–15405, 2019.
12. J.W. Zimmermann, G.E. Hilmas, W.G. Fahrenholtz, *Thermal shock resistance of ZrB_2 and ZrB_2-30% SiC*, Materials Chemistry and Physics, **112**, 1, 140–145, 2008.
13. S.H. Meng, F. Qi, H.B. Chen, Z. Wang, G.H. Bai, *The repeated thermal shock behaviors of a ZrB_2-SiC composite heated by electric resistance*, International Journal of Refractory Metals & Hard Materials, **29**, 1, 44–48, 2011.

14. Z. BALAK, M. AZIZIEH, H. KAFASHAN, A.M. SHAHEDI, Z. AHMADI, *Optimization of effective parameters on thermal shock resistance of ZrB_2-SiC-based composites prepared by SPS: Using Taguchi design*, Materials Chemistry and Physics, **196**, 333–340, 2017.

15. X.H. ZHANG, P. HU, J.C. HAN, S.H. MENG, *Ablation behavior of ZrB_2-SiC ultra high temperature ceramics under simulated atmospheric re-entry conditions*, Composites Science and Technology **68**, 7–8, 1718–1726, 2008.

16. H.W. ZHANG, D.D. JAYASEELAN, I. BOGOMOL, M.J. REECE, C.F. HU, S. GRASSO, W.E. LEE, *A novel microstructural design to improve the oxidation resistance of ZrB_2-SiC ultra-high temperature ceramics (UHTCs)*, Journal of Alloys and Compounds, **785**, 958–964, 2019.

17. A. RADHI, V. LACOBELLIS, K. BEHDINAN, *A passive oxidation, finite element kinetics model of an ultra-high temperature ceramic composite*, Composites Part B-Engineering, **175**, 107129, 2019.

18. Z.Y. WANG, R.T. LI, W.D. SONG, *Dynamic failure and inelastic deformation behavior of SiC ceramic under uniaxial compression*, Ceramics International, **46**, 1, 612–617, 2020.

19. J. VENKATESAN, M.A. IQBAL, V. MADHU, *Experimental and numerical study of the dynamic response of B_4C ceramic under uniaxial compression*, Thin Wall Structure, **154**, 106785, 2020.

20. Y.J. DENG, H. CHEN, X.W. CHEN, Y. YAO, *Dynamic failure behavior analysis of TiB_2-B_4C ceramic composites by split Hopkinson pressure bar testing*, Ceramics International, **47**, 15, 22096–22107, 2021.

21. M. SHAFIQ, G. SUBHASH, *Dynamic deformation characteristics of zirconium diboride-silicon carbide under multi-axial confinement*, International Journal of Impact Engineering, **91**, 158–169, 2016.

22. L.L. WANG, J. LIANG, G.D. FANG, X.Y. WAN, J.B XIE, *Effects of strain rate and temperature on compressive strength and fragment size of ZrB_2-SiC-graphite composites*, Ceramics International, **40**, 4, 5255–5261, 2014.

23. W. HUANG, M. WANG, Z. HU, L.L. WANG, J.X. CAO, D.W. KONG, *Experimental and numerical investigation on strain rate-dependent tensile behavior of ZrB_2-SiC ceramic composite*, Acta Mechanica Solida Sinica, **34**, 137–148, 2021.

24. M. WANG, D.W. KONG, L.L. WANG, Y.B. LI, T. CAI, *Dynamic compressive response of zirconium diboridesilicon carbide composites at highstrain rates*, International Journal of Applied Ceramic Technology, **16**, 6, 2206–2213, 2019.

25. Z.Y. WANG, P.F. LI, *Dynamic failure and fracture mechanism in alumina ceramics: experimental observations and finite element modelling*, Ceramics International, **41**, 10, 12763–12772, 2015.

26. Y.L. LI, S.S. HU, Y.H. LI, *Research on dynamic behaviors of A95 ceramics under compression*, Explosion and Shock Waves, **24**, 233–239, 2004 [in Chinese].

27. J.Z. CHANG, Z.F. LIU, Y.H. LI, Y.L. LI, J.P. LI, *Numerical simulations for dynamic behaviors of A95 ceramic under shock compression*, Journal of Materials Science & Engineering, **4**, 616–619, 2007 [in Chinese].

28. S.A. SILLING, *Reformulation of elasticity theory for discontinuities and long-range forces*, Journal of the Mechanics and Physics of Solids, **48**, 1, 175–209, 2000.

29. S.A. SILLING, E. ASKARI, *A meshfree method based on the peridynamic model of solid mechanics*, Computers & Structures, **83**, 17–18, 1526–1535, 2005.

30. S.A. Silling, E. Askari, *Peridynamic Modeling of Impact Damage*, [in:] F.J. Moody [ed.], American Society of Mechanical Engineers, New York, pp. 197–205, 2004.

31. P. Demmie, S.A. Silling, *An approach to modeling extreme loading of structures using peridynamics*, Journal of Mechanics of Materials and Structures, **2**, 10, 1921–1945, 2007.

32. Y.D. Ha, F. Bobaru, *Characteristics of dynamic brittle fracture captured with peridynamics*, Engineering Fracture Mechanics, **78**, 6, 1156–1168, 2011.

33. Y.D. Ha, F. Bobaru, *Studies of dynamic crack propagation and crack branching with peridynamics*, International Journal of Fracture, **162**, 1, 229–244, 2010.

34. F. Bobaru, G.F. Zhang, *Why do cracks branch? A peridynamic investigation of dynamic brittle fracture*, International Journal of Fracture, **196**, 1–2, 59–98, 2016.

35. J. Lee, J.W. Hong, *Dynamic crack branching and curving in brittle polymers*, International Journal of Solids and Structures, **100–101**, 332–340, 2016.

36. A. Candaş, E. Oterkus, C.E. İmrak, *Dynamic crack propagation and its interaction with micro-cracks in an impact problem*, Journal of Engineering Materials and Technology-Transactions of the ASME, **143**, 1, 011003, 2021.

37. A. Candaş, E. Oterkus, C.E. İmrak, *Peridynamic simulation of dynamic fracture in functionally graded materials subjected to impact load*, Engineering with Computers, **39**, 253–267, 2023.

38. T. Jia, D. Liu, *Simulating wave propagation in SHPB with peridynamics*, [in:] B. Song, D. Casem J. Kimberley [eds.], Dynamic Behavior of Materials, Vol. 1, Conference Proceedings of the Society for Experimental Mechanics Series Springer, Cham, pp. 195–200, 2014.

39. X. Gu, Q. Zhang, D. Huang, Y.T. Yv, *Wave dispersion analysis and simulation method for concrete SHPB test in peridynamics*, Engineering Fracture Mechanics, **160**, 124–137, 2016.

40. D.H. Ai, Y.H. Zhao, Q.F. Wang, C.W. Li, *Experimental and numerical investigation of crack propagation and dynamic properties of rock in SHPB indirect tension test*, International Journal of Impact Engineering, **126**, 135–146, 2019.

41. Y.X. Zhou, K. Xia, X.B. Li, H.B. Li, G.W. Ma, J. Zhao, Z.L. Zhou, F. Dai, *Suggested methods for determining the dynamic strength parameters and mode-I fracture toughness of rock materials*, International Journal of Rock Mechanics and Mining Sciences, **49**, 105–112, 2012.

42. W. Gerstle, N. Sau, S.A. Silling, *Peridynamic modeling of concrete structures*, Nuclear Engineering and Design, **237**, 12–13, 1250–1258, 2007.

43. C.L. Gao, Z.Q. Zhou, Z.H. Li, L.P. Li, S. Cheng, *Peridynamics simulation of surrounding rock damage characteristics during tunnel excavation*, Tunnelling and Underground Space Technology, **97**, 103289, 2020.

44. Y.N. Zhang, H.W. Deng, J.R. Deng, C.J. Liu, B. Ke, *Peridynamics simulation of crack propagation of ring-shaped specimen like rock under dynamic loading*, International Journal of Rock Mechanics and Mining Sciences, **123**, 104093, 2019.

45. C. Diyaroglua, E. Oterkusa, E. Madencib, T. Rabczukc, A. Siddiq, *Peridynamic modeling of composite laminates under explosive loading*, Composite Structures, **144**, 14–23, 2016.

46. Y.L. Hu, N.V. De Carvalhob, E. Madenci, *Peridynamic modeling of delamination growth in composite laminates*, Composite Structures, **132**, 610–620, 2015.

47. L.L. WANG, J.X. CAO, Y.S. ZHAO, X. CHENG, D.W. KONG, *Application situation of peridynamics theory in the study of the failure of brittle materials*, Journal of Guizhou University (Natural Sciences), **38**, 5, 23–30, 2021 [in Chinese].

48. B. REN, C.T. WU, E. ASKARI, *A 3D discontinuous Galerkin finite element method with the bond-based peridynamics model for dynamic brittle failure analysis*, International Journal of Impact Engineering, **99**, 14–25, 2017.

49. Y. AZDOUD, F. HAN, G. LUBINEAU, *The morphing method as a flexible tool for adaptive local/non-local simulation of static fracture*, Computational Mechanics, **54**, 711–722, 2014.

50. H.Z. XING, F. XIE, M.Y. WANG, K.D. XIE, Y.Y. QIU, *Experimental investigation of fracture process zone of rock in dynamic mode I fracturing and its effect on dynamic crack initiation toughness*, Engineering Fracture Mechanics, **275**, 108828, 2022.

51. J.F. KNOTT, *Fundamentals of Fracture Mechanics*, Butterworth, London, 1973.

52. W. YAO, K.W. XIA, *Dynamic notched semi-circle bend (NSCB) method for measuring fracture properties of rocks: Fundamentals and applications*, Journal of Rock Mechanics and Geotechnical Engineering, **11**, 5, 1066–1093, 2019.

53. L. HAI, J.Y. WU, J. LI, *A phase-field damage model with micro inertia effect for the dynamic fracture of quasi-brittle solids*, Engineering Fracture Mechanics, **225**, 106821, 2020.

54. W.M. GUO, Y. YOU, G.J. ZHANG, S.H. WU, H.T. LIN, *Improvement of fracture toughness of ZrB_2-SiC composites with carbon interfaces*, Journal of the European Ceramic Society, **35**, 6, 1985–1989, 2015.

55. P. ZHOU, P. HU, X.H. ZHANG, W.B. HAN, *Laminated ZrB_2-SiC ceramic with improved strength and toughness*, Scripta Materialia, **64**, 3, 276–279, 2011.

56. S.R. LEVINE, E.J. OPILA, M.C. HALBIG, J.D. KISER, M. SINGH, J.A. SALEM, *Evaluation of ultra-high temperature ceramics for aero-propulsion use*, Journal of the European Ceramic Society, **22**, 14–15, 2757–2767, 2002.

57. W.G. FAHRENHOLTZ, G.E. HILMAS, I.G. TALMY, J.A. ZAYKOSKI, *Refractory diborides of zirconium and hafnium*, Journal of the American Ceramic Society, **90**, 5, 1347–1364, 2007.

58. A.L. CHAMBERLAIN, W.G. FAHRENHOLTZ, G.E. HILMAS, D.T. ELLERBY, *High-strength zirconium diboride-based ceramics*, Journal of the American Ceramic Society, **87**, 6, 1170–1172, 2004.

Received December 18, 2022; revised version March 15, 2023.
Published online April 26, 2023.